Acta Geod Geophys (2016) 51:113–123
DOI 10.1007/s40328-015-0114-8

Image-based approach for satellite visibility analysis in critical environments

Jen-Yu Han[1] · **Tsung-Hsien Juan**[1]

Received: 10 February 2015 / Accepted: 16 April 2015 / Published online: 28 April 2015

Abstract The global navigation satellite system (GNSS) positioning solution relies greatly on the satellite configuration visible at a specific receiver location. As a consequence, satellite visibility analysis considering the surrounding terrain obstruction, becomes a key step when the GNSS positioning quality is to be evaluated. Current satellite visibility analysis requires high-resolution digital surface model (DSM) data and is thus a pricey and time-consuming task. In this study, an image-based approach for the satellite visibility analysis is proposed. Terrain obstructions are first identified from photo images, using image-processing techniques. The maximal obstruction angle at each direction is then determined, based on photogrammetric principles. According to the results from a case study, this novel approach provides a satellite visibility analysis solution comparable to that of the current DSM approaches, but with significantly improved computational efficiency. Consequently, a highly efficient and low-cost satellite visibility analysis becomes possible when the proposed approach is implemented.

Keywords Satellite visibility analysis · Global navigation satellite system (GNSS) · Dilution of precision (DOP) · Image classification · Photogrammetric analysis · Sky plot

1 Introduction

The global navigation satellite system (GNSS) is capable of providing high-frequency and accurate positioning and timing solutions across the world, and is thus a common choice for various spatial applications in both scientific and engineering fields. The major observables of this technique are the range measurements between GNSS satellites and

✉ Jen-Yu Han
jyhan@ntu.edu.tw

[1] Department of Civil Engineering, National Taiwan University, 1, Sec. 4, Roosevelt Rd., Taipei 10617, Taiwan

ground receivers. As a consequence, its resulting quality is highly dependent on the network geometry formed by the satellites, and visible to a specific receiver (Leick 2004). The effect of receiver-satellite geometry on the GNSS positioning accuracy is typically quantified by the dilution of precision (DOP) factors, extracted from the covariance matrix in a least-squares adjustment (see e.g., Strang and Borre 1997; Hofmann-Wellenhof et al. 2011; Misra and Enge 2011; Leick 2004). The DOP analysis is thus provided in many commercial software packages. It allows users to predict the positioning quality, or identify weakness in satellite geometry, so that a GNSS field survey can be better planned in advance.

To perform a quality prediction or evaluation on the GNSS positioning solutions, such as in the above mentioned DOP analysis, it requires that the GNSS satellites visible at a pre-defined receiver location should be first identified. In an open area without any terrain obstruction, the predicted satellite orbits (based on given ephemeris) are transformed into a local Cartesian frame, using east-north-up (E-N-U) coordinate components. Those satellites with a positive U coordinate component (i.e. positive elevation angle) are located above the local horizon, and are regarded as visible to the receiver. In the case where terrain obstructions are considered, a masking angle is typically used as a simple criterion, to exclude satellites with a smaller elevation angle which could be obstructed by local topography, such as mountains and buildings. For example, Chiang et al. (2009) adopted a fixed masking angle of 10° and 40° to simulate the terrain obstructions in open sky areas and urban canyons, respectively. This is apparently a rough approach because the fixed masking angle cannot realistically reflect the actual terrain variations, which could cause different levels of obstruction between satellites and receivers. On the other hand, recent advances in spatial techniques allow one to collect detailed 3D topography data across the world, in an efficient manner. High-quality digital terrain models (DTMs) can be produced and continuously updated by aerial photogrammetry, air-borne light detection and ranging (LiDAR), or high-resolution satellite stereo-image techniques (see e.g., Ackermann 1999; Kobler et al. 2007; Hobi and Ginzler 2012; Nurminen et al. 2013). These high-fidelity terrain models give a more realistic topographic representation, and thus facilitate the satellite visibility analysis under topographic obstructions. In recent years, more and more studies have focused their attention on the satellite obstruction analysis, using realistic topographic information. Examples can be found in Taylor et al. (2005), who utilized a triangular irregular network (TIN) created by LiDAR and photogrammetry data, to model the buildings while analysing possible signal obstructions. Besides, Hogan and Santos (2005) studied the data link between the GNSS base and rover stations with a DTM. Li et al. (2006) introduced a ray-tracing model to investigate the GPS multi-path effect, using a high-resolution DSM. Zhang et al. (2008) and Kleijer et al. (2009) adopted high-fidelity city models, to investigate GNSS availability and accuracy in urban areas. More recently, Han et al. (2012) implemented a high-resolution DSM, and developed an approach to determine the optimal site location of GNSS base stations under topographic obstructions. All these previous works with various purposes have demonstrated the advantages of incorporating digital topographical information in a satellite visibility analysis.

Although the inclusion of DTMs contributes to a more reliable analysis of satellite visibility, it also brings up another issue to be tackled. When analysing the topographic obstructions, sampling on all the points on each terrain profile originating from the receiver is required. Consequently, this analysis could be a time-consuming task when a high-resolution digital terrain model is used. This problem will become more significant in a mobile GNSS application, since the receiver's location changes across time, and the obstruction analysis has to be performed repeatedly for every receiver's location. To

overcome this issue, recent studies have also put extra effort into improving the computational efficiency of such an analysis (see e.g., Ackermann et al. 2014; Han et al. 2014). It has been proved that by implementing a proper data structure, or a terrain-sampling algorithm, the computational efficiency can be significantly improved. However, even with these improvements, it still requires dozens of minutes to carry out the satellite visibility analysis, along a simple GNSS survey route. Apparently, there is still much progress to be achieved in order to make this analysis more appealing in practical applications. Finally, it should also be mentioned that high-detailed terrain data is not widely accessible to the general public. In some countries, it is treated as classified information, owing to national security concerns. This creates an additional barrier for civilian users, who also aim to achieve a more reliable topographic obstruction analysis.

In this study, an image-based approach for the satellite visibility analysis is developed. Terrain obstructions are first identified from photo images, using image-processing techniques. The maximal obstruction angle at each direction is then determined based on photogrammetric principles. The goal is to achieve a reliable and efficient terrain obstruction analysis, using widely accessible spatial information, so that this analysis can be applied by general users in various fields.

Fig. 1 Image binarization based on the HSV colour components for the images acquired in various sky conditions

2 Methodology

2.1 Identifying terrain obstructions from photo images

In order to identify terrain obstructions from a given photo image, one needs first to separate the sky from other ground features (e.g., buildings, mountains, etc.). In the daytime, the sky is typically brighter than other ground features in a recorded image. Consequently, the brightness in each image pixel can be used as a primary reference for the judgement. In this study, the colour space of an image is expressed using the hue-saturation-value (HSV) colour model. The H, S, and V values correspond to the perceived colour, colourfulness and brightness in each pixel, respectively. The following criterion is then used to binarize the input image:

$$\begin{cases} \{V(i,j) \geq V_{30\,\%}\} \& \{180^\circ < H(i,j) < 240^\circ \; or \; S(i,j) < 20\,\%\} \Rightarrow B(i,j) = 1 \,(\text{sky pixels}) \\ else \Rightarrow B(i,j) = 0 \,(\text{non - sky pixels}) \end{cases} \tag{1}$$

In Eq. (1), $V(i,j)$, $H(i,j)$, and $S(i,j)$ represent the brightness, perceived colour, and colourfulness values at the pixel location (i,j) in the input image, respectively. $V_{30\%}$ is a threshold value determined based on the top 30 % of the brightness values in the image. $B(i,j)$ is the binarized image. Equation (1) will simply categorize the pixels with top 30 % brightness values and blue ($180^\circ < H(i,j) < 240^\circ$) or white ($S(i,j) < 20$ %) colour responses as potential sky pixels, and others as non-sky pixels. It is found that this empirical criterion can be used to correctly separate the sky pixels for the images acquired on a sunny day or on a cloudy day, even with the presence of scattered clouds in the sky (see Fig. 1). It is thus adopted for the subsequent analyses in this study.

When the potential sky pixels are determined using the above approach, the next step is to identify the definite boundary between the sky and ground obstructions. This can be achieved by employing the Canny edge detection technique (Canny 1986), involving five major steps. First, the image is smoothed by applying a Gaussian filter, so that noises are eliminated. Next, the intensity gradient of the image is computed, and a non-maximum suppression technique is applied, to identify the location of potential edge pixel with the sharpest change of intensity value. Then, double-threshold values are introduced to classify all potential edge pixels into groups of strong-edge pixels, weak-edge pixels, and non-edge pixels. Finally, an edge-tracking technique is performed, so that only the potential edge

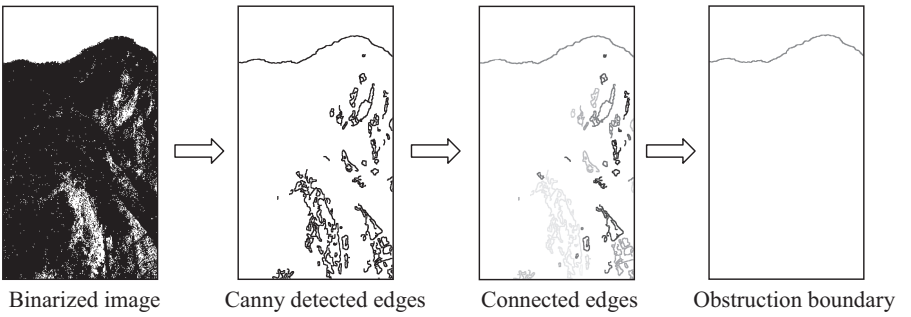

Fig. 2 Identifying boundary between the sky and ground obstructions

pixels connected to the pixels in the strong-edge group are preserved and outputted. After all the edges are identified from the input image, a component labelling approach is applied, so that the edges connected to one another can be grouped further, and each connected group is given a distinct identification label. The connected groups that contain edges reaching both sides of the image are selected as candidate boundaries. Lastly, the candidate in the upmost part of the image is extracted, and outputted as the boundary between the sky and ground obstructions. The images resulting from each major process of the obstruction boundary identification, based on the proposed approach, are illustrated in Fig. 2.

2.2 Estimating maximal obstruction angle at each direction

Once the obstruction boundary points from an image are determined, their elevation and azimuth angles in the object space can be computed based on photogrammetric principles. First, the point coordinates in the image space and object space can be related by the well-known collinearity equation, as follows (Mikhail et al. 2001):

$$\begin{Bmatrix} x - x_0 \\ y - y_0 \\ -f \end{Bmatrix} = k\mathbf{M} \begin{Bmatrix} X - X_L \\ Y - Y_L \\ Z - Z_L \end{Bmatrix} \tag{2}$$

where $\{x \quad y\}^T$ and $\{X \quad Y \quad Z\}^T$ are the coordinate vectors in the image and object space, **M** is the rotation matrix, $\{X_L \quad Y_L \quad Z_L\}^T$ is the translation vector, representing the camera's orientation and location (exposure centre) in the object space, respectively. k is the scale factor from the object space frame to the image space frame, f is the optical focal length, and $\{x_0, y_0\}^T$ is the offset from a fiducial-based origin to a perspective centre origin (Fig. 3).

Based on Eq. (2), the object coordinates for a particular obstruction point in the image space $\{x_i \quad y_i\}^T$ can be written as:

$$\begin{Bmatrix} X_i \\ Y_i \\ Z_i \end{Bmatrix} = \frac{1}{k_i}\mathbf{M}^T \begin{Bmatrix} x_i - x_0 \\ y_i - y_0 \\ -f \end{Bmatrix} + \begin{Bmatrix} X_L \\ Y_L \\ Z_L \end{Bmatrix} \tag{3}$$

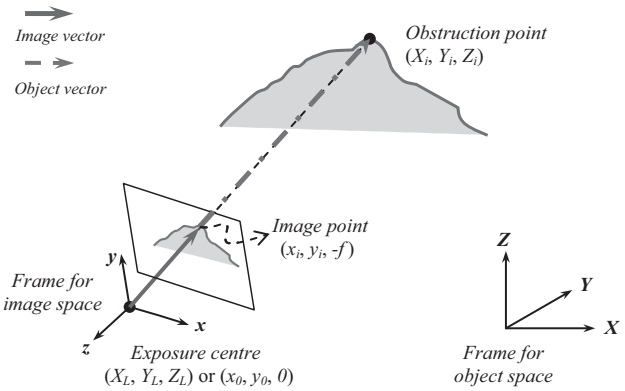

Fig. 3 Geometric relation of point coordinates in the image space and object space

or explicitly,

$$\begin{aligned} X_i &= \frac{1}{k_i}[m_{11}(x_i - x_0) + m_{21}(y_i - y_0) - m_{31}f] + X_L = \frac{A_i}{k_i} + X_L \\ Y_i &= \frac{1}{k_i}[m_{12}(x_i - x_0) + m_{22}(y_i - y_0) - m_{32}f] + Y_L = \frac{B_i}{k_i} + Y_L \\ Z_i &= \frac{1}{k_i}[m_{13}(x_i - x_0) + m_{23}(y_i - y_0) - m_{33}f] + Z_L = \frac{C_i}{k_i} + Z_L \end{aligned} \tag{4}$$

Furthermore, the coordinate differences between the object point and the camera location can be written as:

$$\begin{aligned} dX_i &= X_i - X_L = \frac{A_i}{k_i} \\ dY_i &= Y_i - Y_L = \frac{B_i}{k_i} \\ dZ_i &= Z_i - Z_L = \frac{C_i}{k_i} \end{aligned} \tag{5}$$

In a general application, the frame for object space is typically aligned to the local E-N-U frame (i.e. $dX \equiv dE$; $dY \equiv dN$; $dZ \equiv dU$). Consequently, the elevation angle and corresponding azimuth angle of the object point, with respect to the camera location, can be computed by:

$$El_i = \tan^{-1}\left(\frac{dZ_i}{\sqrt{dX_i^2 + dY_i^2}}\right) = \tan^{-1}\left(\frac{C_i}{\sqrt{A_i^2 + B_i^2}}\right) \tag{6}$$

$$Az_i = \tan^{-1}\left(\frac{dX_i}{dY_i}\right) = \tan^{-1}\left(\frac{A_i}{B_i}\right) \tag{7}$$

After the elevation angles and corresponding azimuth angles of all obstruction points are successively determined, a sky plot representing the terrain obstruction at a ground location can then be obtained, using the following mapping function:

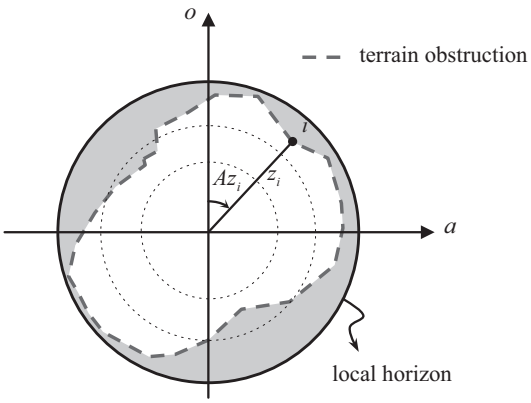

Fig. 4 Sky plot illustrating the satellite visibility condition at a specific ground location

$$a_i := z_i \times \sin Az_i = \left(\frac{\pi}{2} - El_i\right) \sin Az_i \tag{8}$$

$$o_i := z_i \times \cos Az_i = \left(\frac{\pi}{2} - El_i\right) \cos Az_i \tag{9}$$

where z_i is the zenith angle, a_i and o_i are the abscissa and ordinate coordinates of the obstruction point i in the sky plot, respectively (see Fig. 4).

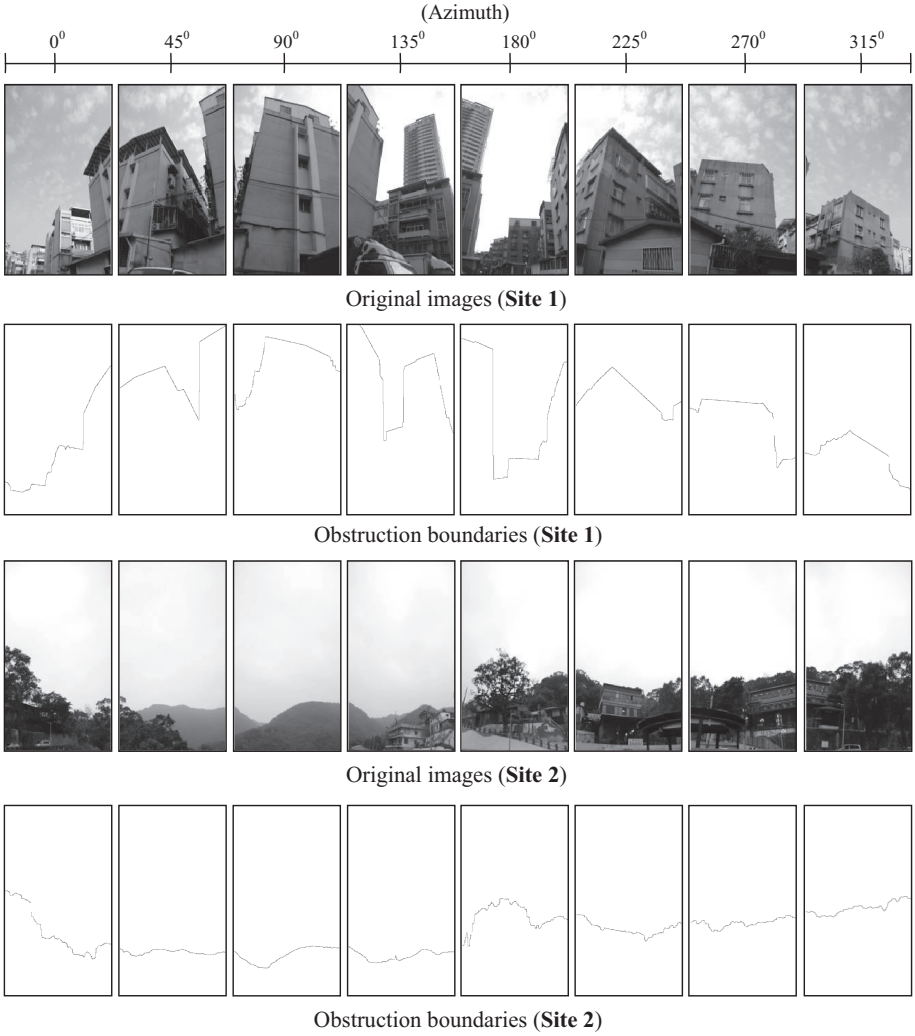

Fig. 5 Raw images and obstruction boundaries for the two test sites

3 Results and discussion

Two test sites were selected for the study. One was located in an urban area surrounded with buildings, and the other one was in a suburb where mountains could cause significant obstructions. A Nikon D-80 nonmetric digital camera was used to acquire the images, with a resolution of 1944 × 2896 pixels. Its horizontal and vertical field of view (FOV) angles were roughly 86° and 64°, respectively. In order to cover as much as possible of the entire view of sky and ground features, the images were taken in portrait mode. As a result, eight images had to be recorded so that the terrain obstructions in all directions could be analysed for that location. The camera was postured with a fixed 0° roll angle and 43° pitch angle. Its yaw angle and coordinates were determined by a digital compass and handheld GNSS device. These camera exterior parameters (orientation and location) were then treated as known constants in the subsequent obstruction analysis.

Figure 5 illustrates the raw images and obstruction boundaries determined, based on the proposed image-processing technique. The image coordinates of the identified obstruction points, together with the known exterior parameter values, were then used to estimate the

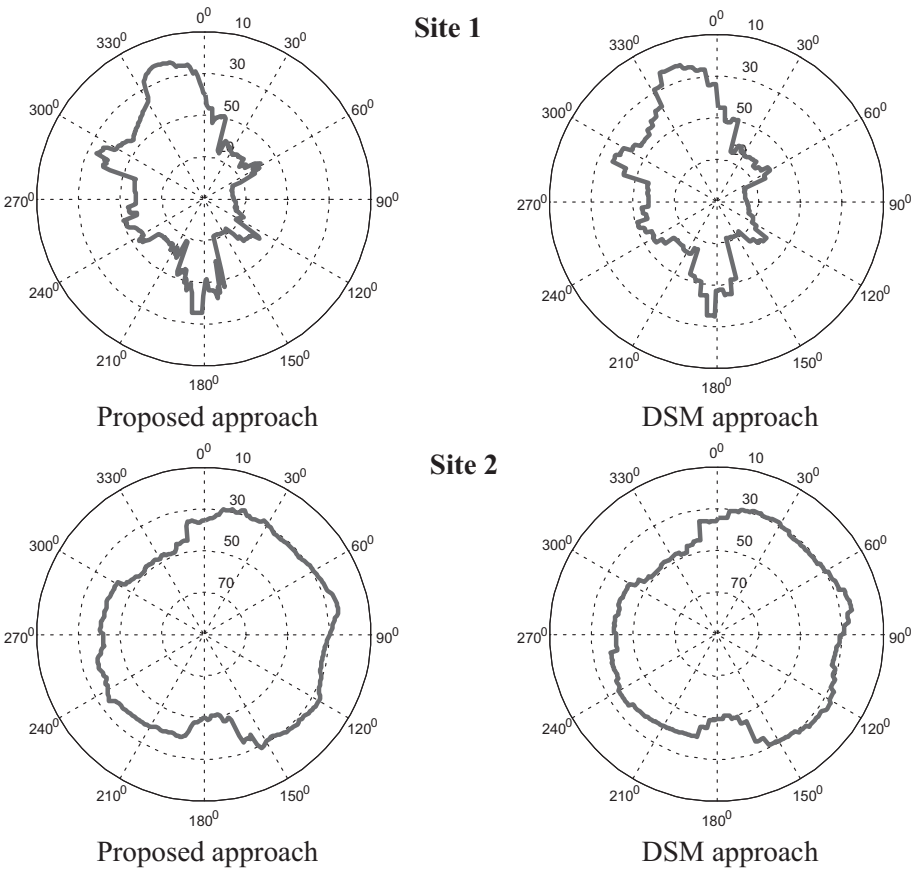

Fig. 6 Sky plots at the two test sites, obtained by proposed image-based approach and classical approach using high-resolution DSM data

Table 1 Comparison of the obstruction analysis results based on the proposed and DSM approaches

	Proposed approach		Comparison (DSM) approach
Site 1			
Processing time	4.05 s		32.58 s
RMSD		1.90°	
Site 2			
Processing time	3.98 s		26.23 s
RMSD		0.89°	

elevation angle and corresponding azimuth angle, based on Eqs. (8) and (9). Finally, the sky plots illustrating the satellite visibility condition at these two test sites could be generated (see Fig. 6). Additionally, in order to evaluate the obtained results, the satellite visibility analysis was also performed at the same locations, but using high-resolution (2 m × 2 m) DSM data covering the test sites. The sky plots obtained, based on this comparison approach, are also illustrated in Fig. 6. The root mean square differences (RMSD) of the obstruction angle at each integer azimuth angle between the two approaches were computed using the following equation, and the results are listed in Table 1. The required processing time (using a consumer grade PC with an Intel Core i7-2600 CPU@3.4 GHz and 8 GB RAM) is also provided in the table. Note that $El_{Az_i,proposed}$ and $El_{Az_i,DSM}$ represent the elevation angles of obstruction points in the azimuth direction Az_i from the proposed and the comparison (DSM) approaches, respectively.

$$RMSD = \sqrt{\frac{\sum_{Az_i=1^\circ}^{360^\circ} \left(El_{Az_i,proposed} - El_{Az_i,DSM}\right)^2}{360}} \tag{10}$$

From the above results, it is clearly illustrated that the terrain obstruction analysis solutions from the proposed image-based approach were similar to those from the classical DSM approach. The RMSD values, representing the elevation angle differences of terrain obstructions at the two test sites, were 1.90° and 0.89°, respectively. When taking the US Global Positioning System as an example, the satellites are roughly 20,200 km away from a ground receiver, and move at a speed of about 3.9 km/sec. This 0.89°–1.90° angular difference corresponds to only a 1.2- to 2.6-min difference for the satellite visible time. Such a difference can be regarded as insignificant in a GNSS filed planning task. Moreover, the required processing time for the proposed approach was only about 12–15 % of that required for the DSM approach. In other words, the proposed image-based approach is capable of achieving a satellite visibility analysis equivalent to that of the classical DSM approach, but with much higher computational efficiency. It also avoids the need for using the high-detailed DSM or other digital terrain data that are usually difficult to access for civilian users.

4 Conclusions

The rapid development of sensor and spatial techniques provides a wide variety of approaches capable of collecting detailed spatial information. Although many alternatives have become available, using an appropriate approach could improve both the efficiency

and reliability of an analysis. In this study, a novel approach for analysing the satellite signal reception under topographic obstructions was developed. This approach successfully integrated image-processing and photogrammetric techniques to identify terrain obstructions, so that visible satellites at any ground receiver can be easily determined. As a consequence, the GNSS positioning quality, or the weakness in satellite geometry, can be realistically estimated. Based on the results of a case study, it has been illustrated that the proposed approach is capable of giving a satellite visibility analysis at the same level of quality as that when using high-resolution digital terrain data. Apparently, the proposed approach is a highly efficient and competitive alternative, because it does not require a huge (3D terrain) dataset or sophisticated algorithm to process it. In other words, complicated satellite visibility analysis will not be limited to the users who possess detailed digital terrain data anymore. Civilian users can easily acquire photo images on their own, and perform the satellite visibility using the proposed approach. Furthermore, it should be mentioned that an image database is now becoming an open source. For example, the Google Street View service is now available in more than 50 countries, comprising data taken along 5 million miles of roads. People are provided with images with a 360° view at many locations free of charge. This further reduces the cost of data acquisition, and gives a strong thrust for extending the satellite visibility analysis to a larger group of general users. With the implementation of the proposed approach, the results produced by modern spatial techniques can actually benefit a wider range of applications in various fields.

Acknowledgments The authors thank the anonymous reviewers for their constructive comments which significantly improved the quality of the original manuscript. The funding support from the Ministry of Science and Technology in Taiwan (under contract No. 103-2221-E-002-128-MY2) is gratefully acknowledged.

References

Ackermann F (1999) Airborne laser scanning: present and future expectations. ISPRS J Photogramm Remote Sens 54:64–67. doi:10.1016/S0924-2716(99)00009-X

Ackermann S, Angrisano A, Del Pizzo S, Gaglione S, Gioia C, Troisi S (2014) Digital surface models for GNSS mission planning in critical environments. J Surv Eng. doi:10.1061/(ASCE)SU.1943-5428.0000119

Canny J (1986) A computational approach to edge detection. IEEE Trans Pattern Anal Mach Intell 8(6):679–698. doi:10.1109/TPAMI.1986.4767851

Chiang KW, Peng WC, Yeh YH, Chen KH (2009) Study of alternative GPS network meteorological sensors in Taiwan: case studies of the plum rains and typhoon Sinlaku. Sensors 9(6):5001–5021. doi:10.3390/s90605001

Han JY, Wu Y, Liu RY (2012) Determining the optimal site location of GNSS base stations. Bol Ciênc Geod 18(1):154–169. doi:10.1590/S1982-21702012000100009

Han JY, Guo J, Chuang JY (2014) Efficient obstruction analysis for the GNSS relative positioning of a terrestrial mobile mapping system. Surv Rev. doi:10.1179/1752270614Y.0000000110

Hobi ML, Ginzler C (2012) Accuracy assessment of digital surface models based on WorldView-2 and ADS80 stereo remote sensing data. Sensors 12:6347–6368. doi:10.3390/s120506347

Hofmann-Wellenhof B, Lichtenegger H, Collins J (2011) GPS theory and practice, 5th edn. Springer, New York

Hogan MK, Santos MC (2005) Advanced mission planning tool for real-time kinematic (RTK) GPS surveying. In: Proceeding of Institute of Navigation National Technical Meeting, San Diego, 24–26 Jan 2005

Kleijer F, Odijk D, Verbree E (2009) Prediction of GNSS availability and accuracy in urban environments—case study Schiphol Airport. Lecture notes in geoinformation and cartography, Springer, New York, pp 387–406. doi: 10.1007/978-3-540-87393-8_23

Kobler A, Pfeifer N, Ogrinc P, Todorovski L, Oštir K, Džeroski S (2007) Repetitive interpolation: a robust algorithm for DTM generation from Aerial Laser Scanner Data in forested terrain. Remote Sens Environ 108(1):9–23. doi:10.1016/j.rse.2006.10.013

Leick A (2004) GPS satellite surveying, 3rd edn. Wiley, New York

Li J, Taylor G, Kidner D, Ware M (2006) Prediction of GPS multipath effect using LiDAR digital surface models and building footprints. Lect Notes Comput Sci 4295:42–53. doi:10.1007/11935148_5

Mikhail EM, Bethel JS, McGlone JC (2001) Introduction to modern photogrammetry. Wiley, New York

Misra P, Enge P (2011) Global positioning system: signals, measurements, and performance. Ganga-Jamuna Press, Lincoln

Nurminen K, Karjalainen M, Yu X, Hyyppä J, Honkavaara E (2013) Performance of dense digital surface models based on image matching in the estimation of plot-level forest variables. ISPRS J Photogramm Remote Sens 83:104–115. doi:10.1016/j.isprsjprs.2013.06.005

Strang G, Borre K (1997) Linear algebra, geodesy, and GPS. Wellesley-Cambridge Press, Wellesley

Taylor G, Li J, Kidner D, Ware M (2005) Surface modeling for GPS satellite visibility. Lect Notes Comput Sci 3833:281–295. doi:10.1007/11599289_24

Zhang K, Liu GJ, Wu F, Densley L, Retscher G (2008) An investigation of the signal performance of the current and future GNSS in typical urban canyons in Australia using a high fidelity 3D urban model. Lecture notes in geoinformation and cartography, Springer, New York, pp 407–420. doi: 10.1007/978-3-540-87393-8_24